OPEN

NPG Asia Materials (2015) 7, e187; doi:10.1038/am.2015.58

www.nature.com/am

ORIGINAL ARTICLE

Nanoporous-gold-based composites: toward tensile ductility

Ke Wang[1], Aaron Kobler[2], Christian Kübel[2], Hans Jelitto[3], Gerold Schneider[3] and Jörg Weissmüller[1,4]

We report on mechanical tests on interpenetrating-phase nanocomposite materials made by vacuum impregnation of nanoscale metal networks with a polymer. The metal component is nanoporous gold made by dealloying, whereas two epoxy resins and polyurethane are explored as the polymer component. The composites are strong and deformable in compression. Although previous observations invariably indicate tensile brittleness for nanoporous gold, composite samples made from cm-sized nanoporous samples enable macroscopic tensile and four-point bending tests that show ductility. This implies that the high strength of individual metal objects such as nanowires can now be incorporated into a strong and ductile material from which macroscopic things can be formed. In fact, a rule-of-mixture-type analysis of the stresses carried by the metal phase suggests quantitative agreement with data reported from separate experiments on small-scale gold nanostructures.
NPG Asia Materials (2015) **7,** e187; doi:10.1038/am.2015.58; published online 12 June 2015

INTRODUCTION

Nanoporous metals made by dealloying[1–3] take the form of monolithic bodies consisting of an interconnected network of nanoscale 'ligaments' in a polycrystalline microstructure with typically 10 to 100 μm grain size.[4,5] The material is under study as a model material for clarifying the deformation mechanisms and mechanical properties of small-scale metal bodies such as nanowires or nanopillars.[5–10] In principle, nanoporous gold (NPG) offers the opportunity of incorporating the extremely high strength that has been reported for individual metal nanostructures, such as nanowires,[6,11–13] into a design strategy for a material that is amenable to the shaping of technologically relevant macroscopic bodies. Yet, whereas micro-scale and, more recently, macroscale nanoporous metal samples show excellent deformability in compression,[5,14] tension and bending studies so far have invariably indicated macroscopically brittle failure.[1,5,15–17] This seems to prevent hopes of applying nanoporous-metal-based materials in technology. The brittle behavior has been linked to a tension-compression asymmetry of the mechanical behavior of porous bodies: while densification of the network implies strain hardening in compression, density loss in tension results in work softening.[18] This latter behavior implies a plastic instability with shear localization and brittle failure in tension. A materials design strategy that prevents the density change under load impregnates is impregnating the pore space with a ductile but lightweight phase, such as a polymer. Compression tests with mm-sized composite samples from NPG and bisphenol-F epoxy confirmed that the impregnation suppresses the density change along with the compressive strain hardening.[18] The compression tests also revealed that the large deformability of NPG and the material's trend of enhanced strength at small ligament sizes are maintained in the composites. Even more interestingly, a first three-point bending test suggested tensile ductility. This points at polymer infiltration of nanoporous metal as a strategy toward a new type of nanocomposite, which exhibits strength and ductility and which has additional technologically interesting features, such as isotropic mechanical response and metallic electric conductivity.

Here we demonstrate that cm-sized samples can be tested in tension. We explore different polymers and show that—depending on the nature of the polymer—good ductility can be achieved. This finding is remarkable in view of the tensile brittleness of nanoporous metal samples in all previous studies. It is also remarkable that the metal reinforcement allows to combine the ductility with an appreciable strength, in excess of 100 MPa.

The effective macroscopic strength, σ^{eff}, of nanoporous metal–polymer composites has been found to considerably exceed that of each of the constituent phases.[18] This statement connects to a tentative rule-of-mixtures approach, in which the nanoscale metal network in the composite maintains the effective, macroscopic strength, σ^{N}, of native (no polymer) monolithic samples of nanoporous metal and in which the polymer component contributes in proportion to its volume fraction, 1-φ, where φ denotes the metal volume fraction, and to the strength, σ^{P}, of bulk polymer[18]

$$\sigma^{\mathrm{eff}} = \sigma^{\mathrm{N}} + (1-\varphi)\ \sigma^{\mathrm{P}}. \qquad (1)$$

As a distinctive feature of the present type of composites, the reinforcing metal phase exists in the form of load-bearing monolithic

[1]Institute of Materials Physics and Technology, Hamburg University of Technology, Hamburg, Germany; [2]Institute of Nanotechnology and Karlsruhe Nano Micro Facility, Karlsruhe Institute of Technology, Eggenstein-Leopoldshafen, Germany; [3]Institute of Advanced Ceramics, Hamburg University of Technology, Hamburg, Germany and [4]Institute of Materials Research, Materials Mechanics, Helmholtz-Zentrum Geesthacht, Geesthacht, Germany
Correspondence: Dr K Wang, Institute of Materials Physics and Technology, Hamburg University of Technology, Eissendorfer Strasse 42 (M), Hamburg 21073, Germany.
E-mail: k.wang@tu-harburg.de
Received 21 January 2015; revised 17 April 2015; accepted 20 April 2015

bulk samples that can be tested, providing experimental data for σ^N. As φ and σ^P are also known, the prediction of the tentative rule of mixtures, Equation (1), may be compared with experimental data for the strength of the composite. This strength has been found to be much higher than the prediction of the simple estimate.[18] The finding is not surprising, as the deformation mode of the metal changes when the pore space is filled with polymer, so that load no longer densifies the metal network and plastic deformation is instead carried by a volume-conserving flow field, similar to conventional massive materials. Here, we discuss the mechanical behavior of the composites in relation to a more appropriate rule-of-mixtures approach.

Our study uses three different polymers, the choice of which was motivated as follows: as the first of our set of polymers, we followed the earlier study of Wang *et al.*[18] in using bisphenol-F epoxy resin as a system with low molecular chain length, promoting low viscosity and good infiltration. Epoxy resins are widely used in industrial applications, and specifically in composite materials,[19–22] as epoxies offer high strength and stiffness along with resistance to environmental degradation. Epoxies also provide good bonds to gold.[23] The second polymer, bisphenol-A epoxy resin, is commercially used for fiber-reinforced composites—for instance, in wind turbine blade manufacturing. One of its distinguishing features is its high strength. The third polymer, polyurethane (PU), is widely used in the production of 'sponge' products and its various formulations cover an extremely wide range of stiffness, hardness and densities.[24] The specific PU (see details below) used here has lower strength than the epoxy resins but considerably higher ductility.

All three polymers use amine groups in the linker molecules. Amine groups are known to form covalent bonds with gold,[23] promoting low polymer–gold interface energy and, therefore, good infiltration of the porous gold with the polymer as well as good adhesion during mechanical deformation.

MATERIALS AND METHODS

Preparation of NPG in this study followed the procedures of Wang *et al.*[18] The $Au_{25}Ag_{75}$ (subscripts: atomic-%) master alloy was prepared by arc-melting, followed by homogenization annealing for 100 h at 850 °C. Cylindrical master alloy samples were obtained by wire drawing to 1.2 mm diameter, followed by cutting to 1.7 mm (for compression test samples) or 20 mm (for tension tests) in length. Some of the alloy ingots were rolled to 1.2 mm-thick sheets and polished on both sides to 1 μm diamond finish. Cuboid master alloy samples for four-point bending test were obtained by cutting these ingots with a wire saw. For recovery, samples were then annealed in vacuum for 3 h at 650 °C.

The conversion of the master alloy into NPG by electrochemical dealloying in 1 M $HClO_4$ used an applied potential of 750 mV versus an Ag/AgCl reference electrode in the same solution. The reference electrode potential was +330 mV versus an Ag/AgCl electrode in saturated KCl solution (World Precision Instruments (Berlin, Germany), +200 mV versus the standard hydrogen electrode), implying a shift of +530 mV versus standard hydrogen electrode. When the current fell to below 10 μA, a potential hold at 850 mV for 3 h led to the completion of dealloying. The samples were then rinsed in ultrapure water and dried in vacuum for 3 days. Some samples were annealed at 300 °C in air for different times to increase the mean ligament size.

Composites were prepared using a vacuum impregnation unit (CitoVaca, Struers, Germany). Molds containing dry samples were evacuated, filled *in situ* with the liquid resin/hardener mixture and the liquid was pushed into the pores by venting the vessel to air. After infiltration, molds filled with resin/hardener mixture were put in an oven in air at 60 °C for 20 min to accelerate the reaction of the resin and the hardener. Surplus polymer was removed by lifting the sample out of the polymer before curing and blotting with a tissue. At least 48 h at room temperature were allowed for curing.

The polymers used in this study were: (1) Bisphenol A epoxy resin (RIMR 135, Hexion Specialty Chemicals, Stuttgart, Germany, the number average molecular weigh $\leqslant 700\,g\,mol^{-1}$) and hardener (RIMH 137, Hexion Specialty Chemicals) at a mass ratio of 10:3; (2) Bisphenol F epoxy resin (BER 20, Buehler, Germany, the number average molecular weigh $\leqslant 700\,g\,mol^{-1}$) and amine hardener (BEH 20, Buehler, Germany) with a mass ratio 4/1; this mixture was heated to 55 °C for impregnation; (3) PU resin (Baytec CC 9803, BaySystems, Oldenburg, Germany) and hardener (Desmodur 9804, BaySystems) with a mass ratio of 1:1. For brevity, we designate the three polymers as RIM, BE and PU, respectively.

An aberration-corrected transmission electron microscope (FEI Titan FEI 80–300) was operated at 300 kV in scanning transmission electron microscopy mode with a nominal spot size of 0.14 nm using a high-angle annular dark-field detector for high-resolution structural characterization of the NPG composite. Transmission electron microscope samples were prepared from the bulk materials using an FEI Strata 400 S focused ion beam system (FEI company, Hillsboro, OR, USA) with an OmniProbe 200 for *in situ* lift-out of the transmission electron microscope lamella. The final polishing of the sample was performed using 5 kV Ga^+ ions.

A scanning electron microscope (SEM; LEO 1530 Gemini, Zeiss, Oberkochen, Germany) operated at 10 kV was used for characterizing the microstructure. Polished surfaces of the composite sample for SEM analysis were prepared by cutting, wet grinding down to 4000 grit SiC paper, diamond polishing to 0.25 μm suspensions and a final step using a water-based lubricating agent with a low-relief polishing cloth on an automated polisher.

Compression tests used a Zwick 1484 testing machine (Zwick GmbH & Co. KG, Ulm, Germany), with cylindrical NPG and composite samples of initial dimensions 1.2 mm diameter and 1.7 mm height and with the elongation

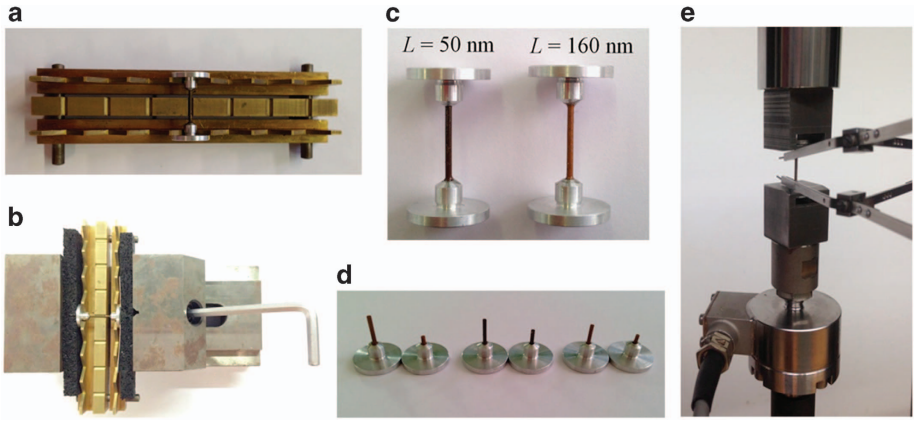

Figure 1 Tensile testing of rod-shaped samples: (**a**) Alignment tool for plane-parallel mounting of holding fixtures. (**b**) Sample being mounted in holding fixtures using a vise. (**c**) Composite sample assemblies, left with ligament size $L = 50$ nm, and right with $L = 160$ nm. (**d**) Fractured samples after testing, note fracture in the center, away from the fixture. (**e**) Sample assembly mounted in the testing rig, using special grips and a clamp-on strain transducer.

measured by an extensometer between the load surfaces. The cuboid samples of polymer of initial dimension $\sim 1 \times 1 \times 1.7\,mm^3$ were cut from bulk samples collected from the same mould as the respective composite samples. True stress, σ_T, and true strain, ε_T, were computed from the elongation by exploiting the findings of constant volume (for epoxy and composite)[18] or constant cross-section (for NPG).[5] A feedback loop controlled and progressively reduced the crosshead speed so as to maintain a constant true strain rate at $10^{-4}\,s^{-1}$ while the sample length varied.

Specimens for tensile testing were prepared as indicated in Figure 1. The rod-shaped samples were glued into Al caps (Figure 1c) using a two-component glue (UHU Plus Endfest 300, UHU GmbH & Co. KG, Bühl, Germany). An alignment bench, Figures 1a and b, assured parallel mounting of the caps. The gauge section was 12 mm in length. Contrary to the circular cross-section of the composite samples, the pure polymer samples used a square cross-section. The samples, of size $1 \times 1 \times 20\,mm^3$, were cut from bulk polymer. Tensile tests were performed in a testing machine (Zwick 1474, Zwick GmbH & Co. KG) with a custom-built grip for the Al caps (Figure 1e) and the elongation of the sample was measured by sensor clips attached to the gauge section (Figure 1e). All tension tests used a strain rate of $10^{-5}\,s^{-1}$.

Four-point bending tests were performed using a custom-built bending rig, originally designed[25] for studies of piezo-ceramics and operated here without the polarization attachment. The inner and outer support roller distances are 10 mm and 20 mm, respectively. The roller diameter is 5 mm. The maximum force and displacement of machine are 75 kN and 1500 μm. The samples here were $1 \times 2 \times 26\,mm^3$ in size, and all surfaces were carefully polished after curing. Beam center displacement and force were measured.

RESULTS

Microstructure

Figure 2 shows high-angle annular dark-field detector-scanning transmission electron microscopy images of thin lamella that were focused ion beam-cut from three RIM-NPG composites of different ligament sizes. The figure illustrates the highly uniform distribution of the two interpenetrating phases and the extremely small structure that can be reached by dealloying. It is also seen that the metal network is regularly connected. For the sample with the largest ligaments, Figure 2c, the lamella thickness is less than the ligament size, so that the connectivity is not represented in the thin cross-section. Due to its low electron density the polymer is not imaged in Figure 2. We now turn to a separate inspection of the polymer distribution.

As a simple but meaningful check of the efficiency of the polymer infiltration, we studied the microstructure of polished sample cross-sections by SEM. For 'native' NPG (no polymer), polishing destroys the fragile ligament structure; the retention of that structure in the composite after polishing therefore testifies to the presence of the polymer phase.[18] Figure 3 compares SEM micrographs for RIM-type composites of different structure sizes in the as-cut (left column) and polished (right column) states. Although images of the as-cut-samples are representative of the microstructure in the composites, the metal phase appears deformed in images of the polished samples. Most importantly, however, the microstructure does not collapse during polishing; this is only possible through the stabilization by the polymer phase, thereby demonstrating complete and uniform infiltration. Analogous tests also confirm complete infiltration for the BE and PU-type composites.

The samples of Figure 3 exhibit different ligament sizes, which are characteristic—from top to bottom in the figure—of the as-prepared state and of coarsened states prepared by annealing the porous metal at 300 °C in air for 2, 5, 10, 30 and 180 min. As representative measure for the characteristic ligament size, L, we took the mean and the variance of sets of at least 20 measurements of the smallest projected ligament diameter on as-cut surfaces. The results are 24 ± 5 nm in the as-prepared material, 54 ± 12 nm after 2 min annealing, 77 ± 13 nm (5 min), 110 ± 30 nm (10 min), 160 ± 30 nm (30 min) and 230 ± 50 nm (180 min). The significant variance in the local ligament diameters in NPG had been previously pointed out based on stereological analysis.[26] Nonetheless the network exhibits a uniform and highly correlated architecture, as evidenced by a pronounced interference peak in small-angle scattering.[27,28]

Compression tests

As a preliminary to the results obtained with composite samples, Figure 4 shows compression stress–strain curves for monolithic samples of the native NPG reinforcement phase alone. The data are partly from Wang *et al.*,[18] obtained with identical procedures as here. The results illustrate the excellent deformability of NPG in compression. Focusing first on as-prepared NPG with the smallest ligament size, $L = 15$ nm, we advertise three distinct regimes of deformation: An initial regime of apparent elasticity is followed by a gradual elastic–plastic transition region, after which the flow stress continuously increases. The strain hardening behavior is unusual in as much as the strain hardening rate increases with increasing strain. For NPG samples with larger L, the apparent elastic regime is suppressed in favor of an immediate onset of plastic deformation. This agrees with previous results in Huber *et al.*[29] and Mameka *et al.*[30] The behavior is here in fact similar to that of well-annealed, macroscopic single crystals of fcc metal.[31]

Figure 5 shows compressive stress–strain curves for the composite materials with different polymers. The graphs are shown for engineering strain values up $\varepsilon_E = 0.5$. All samples could be deformed plastically up to higher nominal strain (at least 0.7) without failure, yet the increasing lateral flow at the high strain and the resulting, multi-axial stress state near the load surfaces prevent a meaningful discussion of the relevant data. Obvious sample barreling was observed after ε_E of $\sim 40\%$.

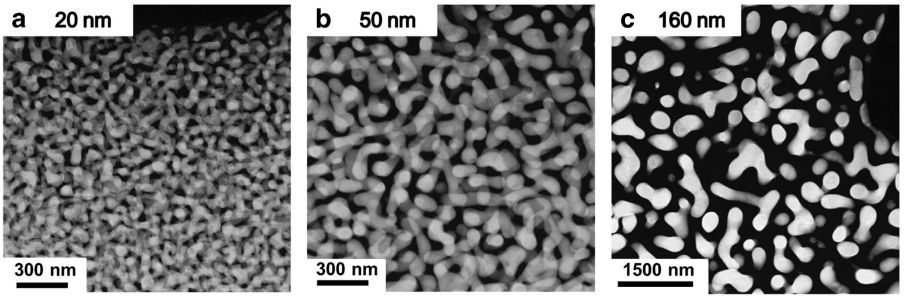

Figure 2 (**a**–**c**) Microstructure of the metal phase in composites of different mean ligament sizes, as indicated by labels. Transmission electron microscopy in high-angle annular dark field imaging mode on samples of nominal thickness ~100 nm. RIM-type composite; see main text for sample designation.

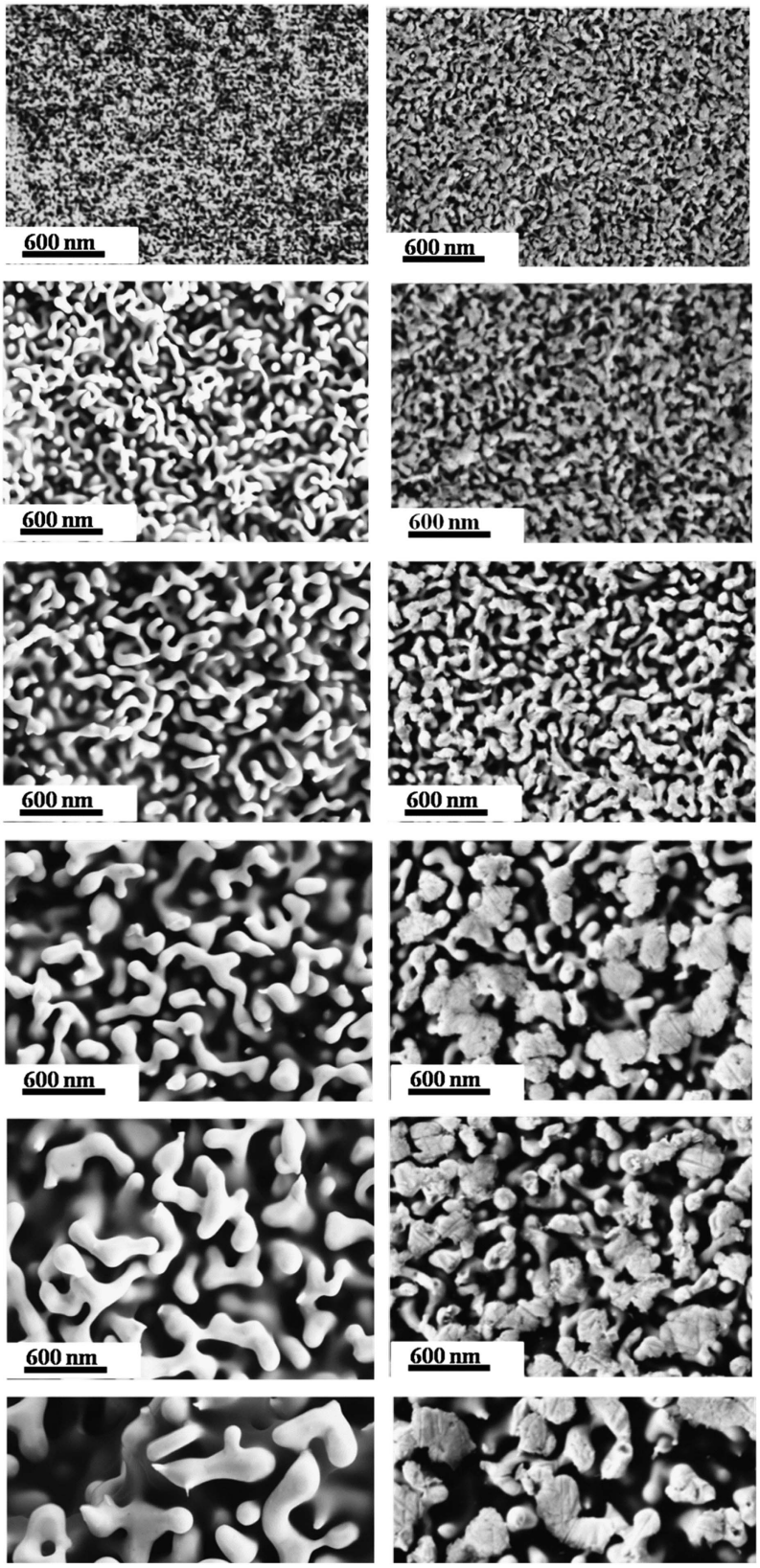

Figure 3 Scanning electron micrographs of original (left column) and polished (right column) cross-sectional cut surfaces of RIM-based composites with mean ligament diameter of about 24 ± 5, 54 ± 12, 77 ± 13, 110 ± 30, 160 ± 30 and 230 ± 50 nm (from top to bottom). Epoxy phase gives no contrast in the SEM and so is not imaged. Note that the ligament structure is conserved in spite of the polishing. This can only be explained by stabilization of the metal microstructure through the interpenetrating epoxy. Integrity of the microstructure on all cross-sections supports complete impregnation.

An exemplary study of the volume change during plastic compression was performed for the BE-based composites.[18] The native NPG samples deformed by densification with no detectable transverse plastic strain. By contrast, the composite was found to deform at essentially constant volume.

For each composite type, the graphs of Figure 5 show stress–strain curves for the respective pure polymer. Yield points are clearly distinguished in the two epoxies, followed by regions of approximately constant flow stress and a final strain hardening stage before failure. The polyurethane behaves similarly except for the absence of a yield point. The strengths vary considerably, with the RIM being strongest, the BE only about half as strong, and the PU again weaker by half.

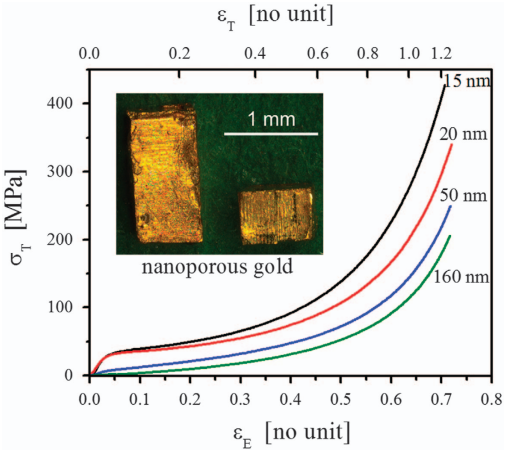

Figure 4 Compression stress–strain curves of true stress, σ_T, versus engineering strain, ε_E, for nanoporous gold at a strain rate of $10^{-4}\,s^{-1}$. The top abscissa shows true strain, ε_T. Data are partly from Wang *et al.*[18]

Turning now to the composite data in Figure 5, we advertise the significantly different stress–strain behavior as compared with native NPG. Yielding is well defined for the RIM- and BE-based samples. The PU-based material exhibits a more gradual elastic–plastic transition, yet its initial stress–strain response is still considerably steeper than for the NPG samples. A more gradual increase in the initial stress of the PU-composite at larger ligament sizes reflects an enhanced initial elastic–plastic compliance of the native NPG samples at larger L.

Contrary to native NPG, the composite samples—and specifically those based on RIM epoxy—show extended regimes of nearly constant flow stress. This confirms our earlier observation of the suppression of densification, which is a source of strain hardening in the pure metal samples.

As one of the central observations in our study, we find for each composite type that the strength increases significantly with decreasing ligament size of the metal phase. This emphasizes that the strengthening of the metal at small structure size is indeed transferred into the composite and that the high strength of nanoscale metal provides an efficient means of strengthening composite materials. For the strongest composite, RIM in $L = 20$ nm NPG, the compressive yield strength reaches 120 MPa.

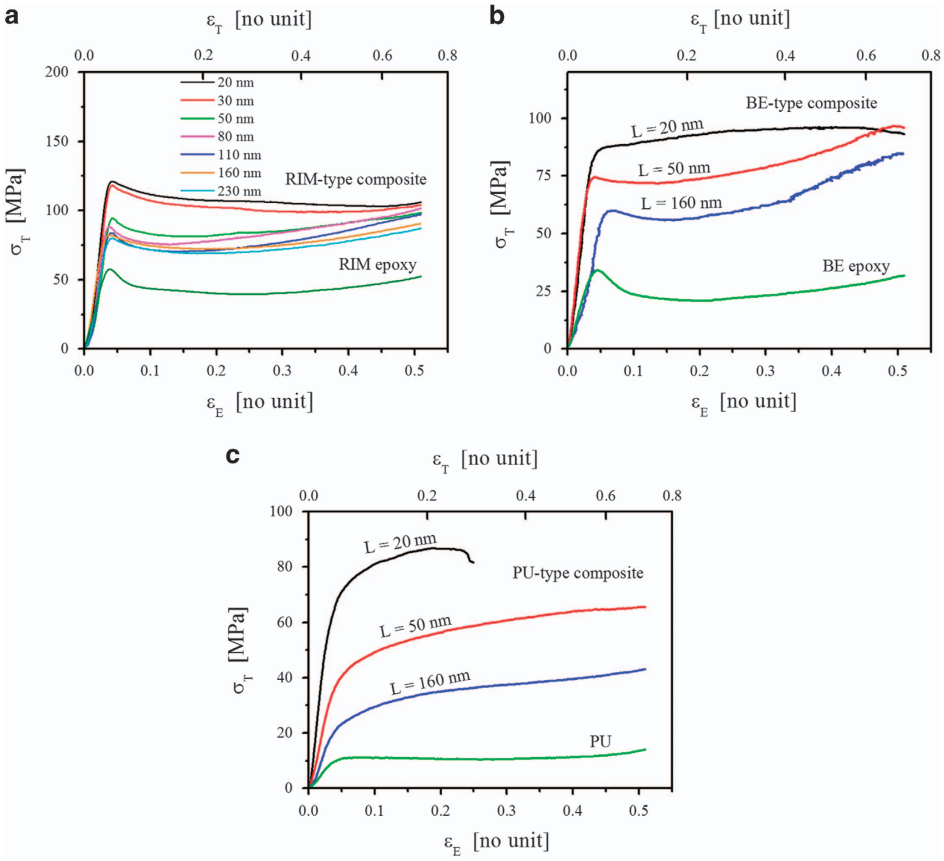

Figure 5 Compression stress–strain curves of true stress, σ_T, versus engineering strain, ε_E, from compression tests on cylinder samples of initial dimension $\sim 1.2\,mm^2 \times 1.7$ mm. True strains, ε_T, are shown on the top abscissa. Data are for composites of (**a**) RIM-type, (**b**) BE-type (data are partly from Wang *et al.*[18]), and (**c**) PU-type, and for the respective pure polymers. Strain rate is $10^{-4}\,s^{-1}$.

The plastic Poisson ratio may be inferred from data for the volume change after compression. For the BE-type composites, compression to $\varepsilon_E = -0.71$ resulted in relative volume changes of $\Delta V/V = -0.046 \pm 0.010$ and -0.030 ± 0.010 at ligament sizes 50 and 150 nm, respectively.[18] The plastic Poisson ratios then emerge as 0.481 ± 0.004 and 0.488 ± 0.004, respectively. Although the deviation from the ideal, volume-conserving value of 1/2 is measurable, its smallness supports the notion that the introduction of the polymer in the pore space suppresses the density change under uniaxial stress almost completely.

Tensile tests

Turning now to tensile testing, we refer to Figure 1c above for the geometry, with cylindrical samples of 1.2 mm in diameter and ~12 mm in gauge length. We start out with tensile stress–strain curves of the pure polymers, Figure 6. Although we find the PU and BE of equal strength in tension and compression, the RIM strength in tension is around 20% less than the compression value. Experiments on pure polymer with different strain rates (not shown) indicate that the strain-rate sensitivity of RIM is stronger than that of PU. It is thus likely that the different strengths of RIM relate to the different strain rates, $10^{-4}\,s^{-1}$ in the compression test versus $10^{-5}\,s^{-1}$ during tension. All polymers can be deformed to large strain in tension.

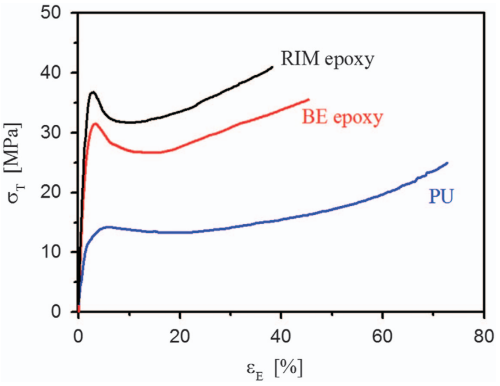

Figure 6 Tensile stress–strain curves of true stress, σ_T, versus engineering strain, ε_E, for RIM, BE and PU polymer samples with gauge section $1 \times 1 \times 12\,mm^3$ at strain rate $10^{-5}\,s^{-1}$.

The tensile tests on the composite samples studied ligament sizes of 50 and 160 nm. Stress–strain graphs are shown in Figure 7. It is seen that composite specimens of all three types exhibit a well-defined elastic regime, followed by a curved stress–strain graph that indicates a transition to plastic deformation. The plastic strain to failure is quite small for the RIM samples, but the BE sample with $L = 160$ nm and all PU samples show appreciable strain, reaching ~10% for the PU-composite specimen with $L = 160$ nm.

As was already found in the compression tests, the composites are considerably stronger in tension compared with their pure epoxy counterparts. For instance, the 0.2% yield stress of RIM epoxy-NPG with L of 50 nm is around threefold larger than that of pure RIM epoxy. Furthermore, we again find that the apparent yield stress increases with decreasing ligament size. All three composites are stronger in our compression experiment compared with the tension tests. The difference has a natural explanation in the slower strain rate of the tension tests. Compression tests on the composites (not shown) indicate a significant strain rate sensitivity, consistent with the generic strain rate sensitivity of polymers.

Tests with several nominally identical samples found failure mostly within the gauge section, with only occasional failure events at the

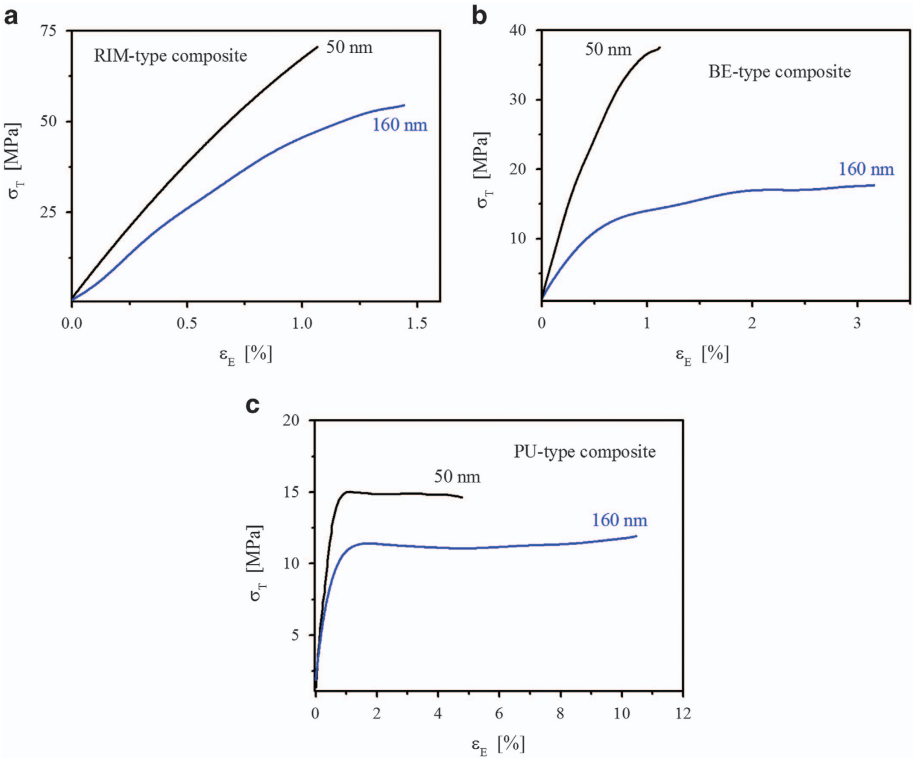

Figure 7 Tensile stress–strain curves of true stress, σ_T, versus engineering strain, ε_E, for samples with gauge section $1.2\,mm^2 \times 12$ mm. (**a**) RIM-type composites; (**b**) BE-type composites; (**c**) PU-type composites. Mean ligament sizes are indicated in the figure. Strain rate is $10^{-5}\,s^{-1}$.

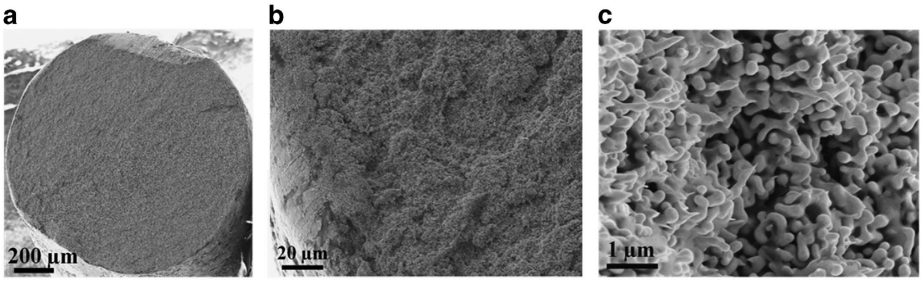

Figure 8 Scanning electron micrograph of the fracture surface of an as-tested RIM-type composite sample with ligament size 160 nm from the tensile test. Magnification increases from **a** to **c**. The fracture surface is at 90° angle to load axis.

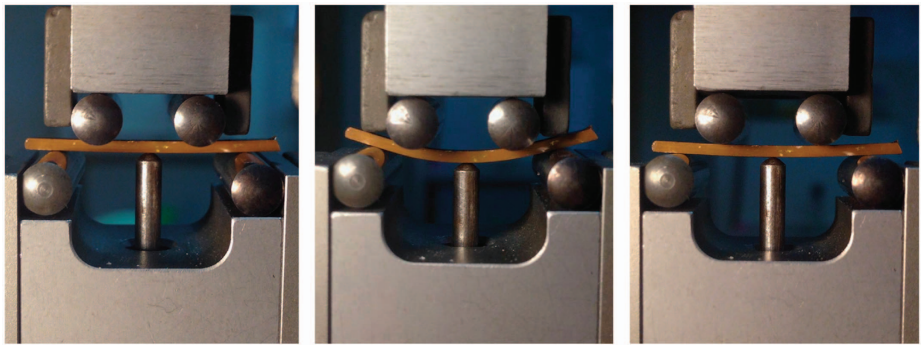

Figure 9 Photographs of four-point bending test with a RIM-type composite sample of ligament size 160 nm. Left, before loading; center, at maximum load; right, after unloading. Note the large deformability and the almost complete recovery.

gripping shoulder. The prevailing failure location is apparent in Figure 1d. Figure 8 shows SEM micrographs of an exemplary fracture surface (RIM-based composite, ligament size 160 nm). The failure on a cross-sectional surface perpendicular to the load axis (Figure 8a) is characteristic of cleavage fracture. An inclined region on the fracture surface might be related to crack initiation. This type of feature was found in several fractured samples. Close inspection reveals a small waist along the circumference, indicating that localized plastic deformation may have preceded the failure. This would be consistent with the work softening immediately after the yield point, as evidenced by the compression tests of Figure 5a. The higher magnification image of the fracture surface in Figure 8b shows roughness at the scale of tens of microns and below, conceivably linked to variations in the local structure and strength of the reinforcing metal network structure. At even higher magnification, Figure 8c, it is apparent that the individual reinforcing metal ligaments have undergone large plastic deformation before fracture, as evidenced by the formation of sharp cusps at the points of failure.[15,17]

Four-point bending test

Four-point bending experiments were performed on RIM-NPG composite samples with $L = 160$ nm. Photographs of the experiment at the non-deformed, maximum bending and final unloaded states (from left to right) are shown in Figure 9. The central picture of Figure 9 shows the composite sample deformed to the maximum displacement of the bending rig. This was possible with no apparent failure.

The graph of force, F, versus displacement, δ, in the beam center during bending (Figure 10a) is linear, suggesting that the linear behavior of the Euler–Bernoulli beam theory[32,33] is an acceptable approximation to our data. The stress, σ, is then related to the load, F, and to the geometry by[34]

$$\sigma = \frac{3Fa}{bh^2}, \tag{2}$$

where b and h are the width and height of the sample and a represents the distance between the outer and inner support rollers. Furthermore, the displacement satisfies[34]

$$\delta = \frac{Fa}{48YI(3L^2 - 4a^2)} \tag{3}$$

with Y the Young's modulus, I the moment of inertia ($I = bh^3/12$), and L the length of the outer loading span. Using Hooke's law with Equations (2) and (3) gives

$$\varepsilon = \frac{12\delta h}{(3L^2 - 4a^2)}. \tag{4}$$

for the strain in the outer fiber.

The outer fiber stress–strain curve, as evaluated on the basis of the F-δ curve according to Equations (2) and (4), is shown in Figure 10b. It is seen that, at the maximum measuring range, the sample could be deformed elastically and without failure to 2.0% strain, at which time the stress reached 140 MPa. This is considerably stronger than the corresponding tensile test result (Figure 7a).

DISCUSSIONS

The most obvious findings of this work are (i) the very substantial strengthening of all polymers under investigation by incorporation of the reinforcing nanoporous metal phase, and (ii) the tensile ductility of the composite samples, which contrasts with the brittle tensile

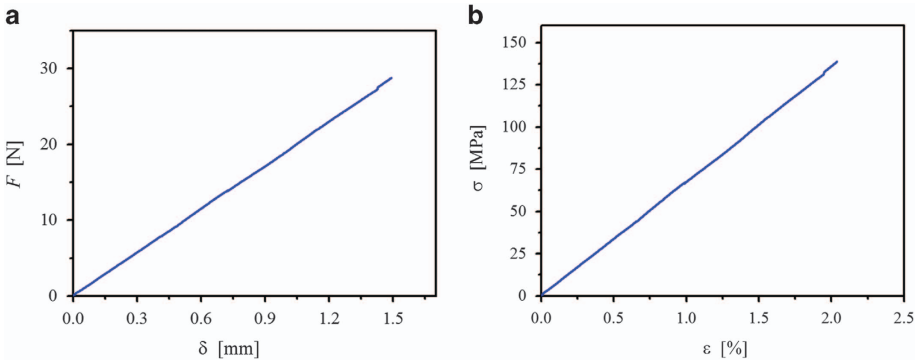

Figure 10 (**a**) Graph of force, F, versus displacement, δ, during four-point bending measurement. (**b**) Stress, σ, versus strain, ε, in the most tensile fiber as computed with Equations (2) and (4).

behavior of the pure nanoporous metal. The discussion will focus on the mechanical properties of the composites, as the behavior of the pure metal has already been discussed in previous work (see Introduction).

Compressive plastic deformation

From Figure 5, it is apparent that all materials exhibit excellent deformability in compression. The strength of the composites at any given L follows the trends of the polymer strengths, with RIM composites stronger than BE- and then PU-based composites. Furthermore, the characteristics of the composites also follow the trend of 'smaller is stronger' for the metal phase that is so clearly confirmed by the porous metal samples. Finally, the strength of the composites also exceeds those of the constituent materials—namely, NPG and polymer—at any L.

An alternate rule of mixture

It is of interest to separate the contributions of the polymer matrix and of the embedded metal network to the net load carried by the composite. For elastic deformation this is a classic problem of heterogeneous medium theory, with approximate solutions in the form of, for instance, the Hashin Shtrikman bounds.[35] Here our attention is on the plastic deformation, which is open to a simpler, if also approximate, analysis.

The key observation is that, as interconnected networks of nanoscale metal ligaments that are infiltrated with a polymer, our materials are interpenetrating-phase composites. The reinforcing nanoscale metal network on its own thus forms monolithic samples that can be tested (see our results in Figure 4). As the experiment puts the strength of the composites several times higher than either the pure nanoporous metal or the pure polymer, a rule of mixture based on the weighted sum of the strength of the individual phases, as in Equation (1), does not appropriately describe the mechanical behavior of the composite.

The failure of Equation (1) is not surprising, as filling the pore space with the polymer changes the mode of the deformation of the nanoscale metal network. While compression of the pure nanoporous metal is entirely carried by densification, plastic flow of the composite material at constant effective macroscopic flow stress involves a volume-conserving flow field. In fact, plastic flow of the bicontinuous microstructure is consistent with metal and composite deforming coherently with uniform and identical values of the strain rate, $\dot{\varepsilon}$, in each phase. This flow field is also consistent with constant (but not necessarily uniform) stress at each material point in each phase and, therefore, with a volume-conserving flow. In fiber-reinforced composites, relaxation at the fiber ends and slip at the fiber–polymer interface are well known to imply a significant deviation from the uniform strain rate. This imposes a correction, for instance, by a 'strength efficiency factor'.[36] Furthermore, the essentially brittle behavior of classic reinforcements such as carbon fibers prevents the coherent plastic deformation of polymer matrix and fibres, leading to failure at small plastic strain. The present material presents a more benign case for analysis, as both constituent phases are locally ductile, and as the requirement of maintaining contiguity in the bicontinuous microstructure enforces the plastic flow to be coherent.

Our material is macroscopically isotropic and we may here assume that this isotropy can be carried over to the local flow field. In doing so we ignore the crystalline anisotropy of the metal in each of the randomly oriented grains (a few tens of micron in size)[5] of the metal microstructure. The assumption appears reasonable, as the metal microstructure in the composite is inherited from NPG and as NPG does deform uniformly at the micron scale.[5]

If we accept the flow field as volume-conserving and the material as isotropic, then the uniaxial load simply leads (in an orthonormal coordinate system aligned with the load axis) to a strain rate tensor, $\dot{\mathrm{E}}$, according to

$$\dot{\mathrm{E}} = \dot{\varepsilon}\begin{pmatrix} -\frac{1}{2} & 0 & 0 \\ 0 & -\frac{1}{2} & 0 \\ 0 & 0 & 1 \end{pmatrix}. \tag{5}$$

In other words, the plastic flow is parameterized by the scalar strain $\dot{\varepsilon}$ rate alone, and is therefore identical to that in a pure polymer sample deformed at the same strain rate.

Our tests use identical strain rates for the composite samples and the pure polymer samples. As it is reasonable to assume that the stress in the polymer phase of the composites is governed by the strain rate, we conclude that this stress is identical for the composite and pure polymer samples in our experiments. This allows us to exploit our pure polymer experiments for identifying the stress, σ^{P}, in the polymer phase of the composite.

Once the stress in the polymer phase is estimated from experiments on pure polymer, we can use a simple balance-of-force argument for relating the effective flow stress of the composite, σ^{eff}, to the solid fraction, φ, and to the stresses, σ^{M} and σ^{P}, in the metal and polymer phases. To this end we decompose the net load, T, on a cut surface (area A) through the composite, normal to the load axis, into contributions from metal and polymer according to the rule of mixture

$$T/A = \sigma^{\mathrm{eff}} = [\varphi\ \ \sigma^{\mathrm{M}} + (1-\varphi)\ \ \sigma^{\mathrm{P}}]. \tag{6}$$

This ansatz exploits that the area fractions of the phases on a

representative cut surface agree with their respective volume fractions in bulk. An equation analogous to Equation (6) is known to apply to the axial strength of fiber-reinforced composites in the limit of very long aligned fibers.[36]

The consistency of Equation (6) with our data may be checked by inspecting its implications for the strength of the metal ligaments. To this end, Equation (6) is rearranged into

$$\sigma^{M} = [\sigma^{eff} - (1-\varphi)\ \sigma^{P}]/\varphi, \qquad (7)$$

which affords a computation of the metal flow stress from the data for σ^{eff} and σ^{P} that are measured for the composite and pure polymer samples, respectively. The φ values for samples with different ligament sizes have been explored previously for samples made under identical conditions.[18] The as-prepared porous metal has $\varphi = 0.27$, and densification during coarsening leads to $\varphi = 0.29$ and 0.42 for samples with L of 50 nm and 160 nm, respectively.

Figure 11 shows σ^{M} obtained by evaluating data from Figure 5 by means of Equation (7). The stresses are for net engineering strain $\varepsilon_E = 0.1$, the smallest strain value where the flow stress of all composite samples first reaches a nearly stationary value. It is seen that samples with ligament size $L = 20$ and 50 nm give values of σ^{M} that agree closely (the data for all three composites at $L = 20$ nm actually superimpose in the graph), independent of the nature of the polymer. For $L = 160$ nm the deviation is larger, but the general trends for the size dependence are still consistent for all composite types. This finding supports the notion that the flow stress σ^{M} is characteristic of the metal, and it is also supportive of the stress decomposition strategy as embodied in Equation (6).

Figure 11 also includes data for the strength of NPG ligaments that are estimated from the compression and microhardness tests of Jin *et al.*[5] (We work with the data of Figure 3b of Jin *et al.*[5] As indicated there, the Gibson-Ashby scaling relation for the strength, $\sigma^{eff} = 0.3\sigma^{M}\varphi^{3/2}$, was used to estimate the local strength of the metal ligaments from the effective macroscopic mechanical behavior.) It is seen that the estimated metal flow stresses of our composites are closely similar to those estimated for pure NPG, and in particular the trend of smaller is stronger is reflected in the composite. Overall, this finding gives further support to our data analysis.

Closer inspection of Figure 11 shows that the size dependence of strength in the composite is somewhat less than what is inferred from

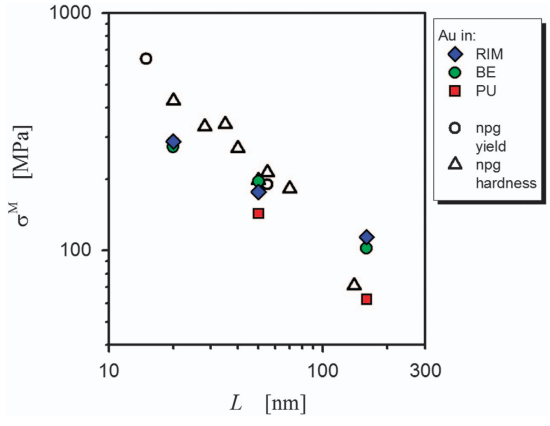

Figure 11 Flow stress, σ^{M}, in the metal versus ligament size, L. Closed symbols, flow stress in the metal phase of the composite samples (for composite types indicated by labels), as obtained by evaluating data from Figure 5 with Equation (7). Open symbols, data from Jin, H.J. *et al.*[5], yield strength from compression tests (label 'yield') and from microhardness (label 'hardness') for nanoporous gold.

pure NPG. One might speculate on a dependency of the polymer properties on the ligament size, which is ignored in our data analysis. Reconciling the data for strength derived from composite samples and that derived from pure NPG in this way would require that the polymer phase in the composite at small ligament size be weaker than bulk polymer. A weakening at small ligament size might be understood in terms of incomplete curing. This might result from depletion of the resin/hardener mixture in hardener because the hardener molecules would be adsorbed at the ligament surface. The adsorption of hardener on gold has been investigated in detail by Aufray *et al.*[23] The small-L composites have more surface area per volume and may, therefore, be more prone to this process. In fact, examining the material with $L = 40$ nm as an example and using the supplier's data for the number-density of amine groups in the hardener (amine value for RIM is 600 mg KOH/g or 1.0×10^{-5} mol amine groups per gram of hardener), we find that the resin in the pore space contains 300 times fewer hardener molecules than Au surface atoms. This implies that, in principle, all hardener molecules could entirely be withdrawn from the resin by adsorption on the Au surface. Obviously, that extreme scenario is not compatible with the mechanical strength of the composite samples in our study. Yet, the finding—in Figure 11—of a reduced apparent strength of the polymer component does support a certain degree of hardener depletion at small L. Studies with systematic addition of extra hardener are in preparation to explore this issue.

While our analysis finds σ^{M} values of a magnitude consistent with Jin *et al.*,[5] where the synthesis protocol and compression sample geometry were identical to our work, it should also be noted that previous work had inferred considerably higher strength for ligaments in NPG as well as for other gold nano- and microstructures.[6–9,37–45] Jin *et al.*[5] linked the discrepancy to inconsistency, in some of these references, in the choice of the Tabor factor[15] when converting nanoindentation hardness data of native NPG to yield stress. Use of the conventional $\sigma^{Y} = H/3$ was found to provide good agreement between hardness and yield strength, while suggesting a downward correction of some of the previous data for the strength of NPG ligaments.[5]

Tensile behavior

Earlier studies found that individual metal ligaments in native NPG undergo large plastic deformation before fracture.[15,17] Our results confirm this finding. More importantly, however, tensile and bending tests on micron- or millimeter-sized NPG samples so far invariably revealed an overall brittle failure at the specimen level.[5,15,17] This was first apparent in the study on fracture behavior in three-point bending tests by Li *et al.*,[1] and the brittleness in bending was later confirmed by Biener *et al.*[17] Balk and coworkers[15,16] tested small volumes in tension,

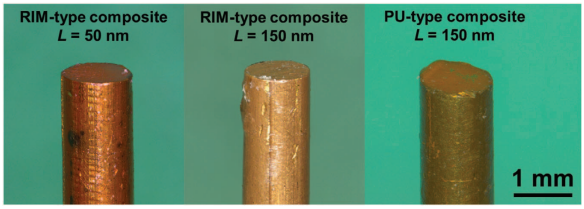

Figure 12 Photographs of composite samples fractured during tension tests. Top surfaces are fracture surfaces. RIM- and PU-type composite samples of different ligament sizes, as indicated in the figure. Note grooves and surface defects resulting from wire-drawing of the master alloy or from handling the nanoporous gold samples before infiltration with polymer.

also finding little to no plasticity. The macroscopic brittleness contrasts with the local behavior of the individual ligaments, which undergo ductile necking before local failure.[15,17] Figure 8c illustrates this behavior for our material.

In stark contrast to the macroscopically brittle behavior of NPG, the tensile tests on our composite specimens for the first time demonstrate tensile ductility in a nanoporous-metal-based material. In fact, as shown in Figure 7, all composite specimens of our work exhibit plastic deformation. This distinguishes the deformation behavior of the nanoporous-metal-based composites qualitatively from that of native NPG.

For composite specimens of all three types, it is seen that the amount of plastic deformation before failure increases with increasing ligament size. This follows the trend of more ductility at lesser strength, which is generic to structural materials.

It is noteworthy that Biener and coworkers reported a mixture of transgranular and intergranular fracture in native NPG.[17] By contrast, fracture surfaces of our tensile composite specimens, such as Figure 8, gave no indication of intergranular fracture. This supports previous results[5,46] suggesting that grain boundaries in appropriately dealloyed NPG samples are not regions of preferred failure and so do not weaken the material.

However, the tensile strength and strain to failure of our material leave room for improvement. It appears natural to speculate on the impact of the surface finish of our samples on their failure. In fact, optical micrographs of fractured samples, Figure 12, show surface grooves from wire-drawing and small defects from handling the NPG samples before infiltration with the polymer. So far, the circular rod geometry of the tensile specimens has prevented us from applying a satisfactory polish.

Samples of rectangular shape are more amenable to high-definition polishing. This was exploited in our four-point bending measurement. On comparing tensile fracture stress and strain of the RIM-NPG composite with L of 160 nm in Figure 7a with the stress value in the same material in maximum bending state under four-point loading (Figure 10b), we found that the polished sample of the bending test is stronger than the non-polished wire-shaped sample tested in tension. The four-point bending test ended in the elastic regime with further deformation prevented by the limitation of the measuring range of the testing rig. Experiments with an improved bending geometry are in preparation and one may expect that interesting deformability characteristics may emerge. Even the present, preliminary results strongly support that polishing enhances the material's performance, and that the ductility in our tensile tests is thus not limited by intrinsic material behavior but is instead extrinsic and due to surface flaws in the specific samples of the test.

CONCLUSIONS

This work systematically studied the mechanical behavior of a novel type of interpenetrating-phase nanocomposite material that exploits the high strength of metal nanostructures. We have described a procedure for preparing and testing cm-sized samples of NPG-based composite materials in tension. The implications of the results, along with those of more conventional compression tests, can be summarized as follows.

Compared with the behavior of pure NPG, the composite has significantly improved tensile ductility as well as a drastic increase in strength in both tension and compression. The flow stress can be decomposed into components from polymer and metal, and the results are well compatible with the trends of flow stress versus ligament size derived from tests on the nanoporous metal.

The observation of tensile ductility is the most significant finding of our study, as all previous tensile tests on nanoporous metal found brittle failure. The fracture strain of our samples increases with increasing ligament size and the ductility of interpenetrating polymer phase. Particularly noteworthy is the large fracture strain of the PU-based composites.

The plastic deformation behavior of our interpenetrating-phase nanocomposites is quantitatively consistent with a simple rule of mixture in which the two phases deform coherently and in which the stress carried by the reinforcing metal phase agrees with the local flow stress of the nanoscale metal ligaments, as deduced from independent measurements on nanoscale metal samples.

Besides demonstrating how nanoporous metal can be incorporated into a materials design scheme that yields ductility in materials that were so far invariably found brittle in tension, our work also has a wider implication in the field of small-scale plasticity. It has been well documented that individual, nanoscale metal bodies can reach extremely high strength.[6,11–13] This raises the obvious question: can the favorable mechanical behavior at the nanoscale be exploited for making strong bodies of technologically relevant, macroscopic dimensions? Our results show a pathway toward that goal by implementing the high strength of nanoscale metal objects in a design strategy that yields strength and ductility in a *material*, in the sense of a substance from which macroscopic things can be formed.

CONFLICT OF INTEREST

The authors declare no conflict of interest.

ACKNOWLEDGEMENTS

This work was funded by DFG through SFB 986 'Tailor-Made Multi-Scale Materials Systems—M3', sub-projects B2 and A6. We thank R Prang (KIT) for the transmission electron microscope sample preparation and K Schulte (TUHH) for helpful discussions.

1 Li, R. & Sieradzki, K. Ductile-Brittle Transition in Random Porous Au. *Phys. Rev. Lett.* **68**, 1168–1171 (1992).
2 Erlebacher, J., Aziz, M. J., Karma, A., Dimitrov, N. & Sieradzki, K. Evolution of nanoporosity in dealloying. *Nature* **410**, 450–453 (2001).
3 Weissmueller, J., Newman, R. C., Jin, H. J., Hodge, A. M. & Kysar, J. W. Nanoporous metals by alloy corrosion: formation and mechanical properties. *Mrs Bull.* **34**, 577–586 (2009).
4 Parida, S., Kramer, D., Volkert, C. A., Rösner, H., Erlebacher, J. & Weissmüller, J. Volume change during the formation of nanoporous gold by dealloying. *Phys. Rev. Lett.* **97**, 035504 (2006).
5 Jin, H. J., Kurmanaeva, L., Schmauch, J., Rosner, H., Ivanisenko, Y. & Weissmüller, J. Deforming nanoporous metal: Role of lattice coherency. *Acta Mater.* **57**, 2665–2672 (2009).
6 Volkert, C. A., Lilleodden, E. T., Kramer, D. & Weissmueller, J. Approaching the theoretical strength in nanoporous Au. *Appl. Phys. Lett.* **89**, 061920 (2006).
7 Biener, J., Hodge, A. M., Hayes, J. R., Volkert, C. A., Zepeda-Ruiz, L. A., Hamza, A. V. & Abraham, F.F. Size effects on the mechanical behavior of nanoporous Au. *Nano Lett.* **6**, 2379–2382 (2006).
8 Biener, J., Hodge, A. M., Hamza, A. V., Hsiung, L. M. & Satcher, J. H. Nanoporous Au: A high yield strength material. *J. Appl. Phys.* **97**, 024301 (2005).
9 Hodge, A. M., Biener, J., Hayes, J. R., Bythrow, P. M., Volkert, C. A. & Hamza, A. V. Scaling equation for yield strength of nanoporous open-cell foams. *Acta Mater.* **55**, 1343–1349 (2007).
10 Biener, J., Wittstock, A., Baumann, T. F., Weissmüller, J., Bäumer, M. & Hamza, a.V. Surface chemistry in nanoscale materials. *Materials* **2**, 2404–2428 (2009).
11 Uchic, M. D., Dimiduk, D. M., Florando, J. N. & Nix, W. D. Sample dimensions influence strength and crystal plasticity. *Science* **305**, 986–989 (2004).
12 Greer, J. R., Oliver, W. C. & Nix, W. D. Size dependence of mechanical properties of gold at the micron scale in the absence of strain gradients. *Acta Mater.* **53**, 1821–1830 (2005).
13 Greer, J. R. & Hosson, J. T. M. D. Plasticity in small-sized metallic systems: intrinsic versus extrinsic size effect. *Prog. Mater. Sci.* **56**, 654 (2011).
14 Jin, H. J. & Weissmueller, J. A material with electrically tunable strength and flow stress. *Science* **332**, 1179–1182 (2011).

15 Balk, T. J., Eberl, C., Sun, Y., Hemker, K. J. & Gianola, D. S. Tensile and Compressive Microspecimen Testing of Bulk Nanoporous Gold. *JOM* **61**, 26–31 (2009).
16 Briot, N.J., Kennerknecht, T., Eberl, C. & Balk, T.J. Mechanical properties of bulk single crystalline nanoporous gold investigated by millimetre-scale tension and compression testing. *Philos. Mag.* **94**, 847–866 (2014).
17 Biener, J., Hodge, A. M. & Hamza, A. V. Microscopic failure behavior of nanoporous gold. *Appl. Phys. Lett.* **87**, 1219081–1219083 (2005).
18 Wang, K. & Weissmuller, J. Composites of Nanoporous Gold and Polymer. *Adv. Mater.* **25**, 1280–1284 (2013).
19 Gojny, F. H., Wichmann, M. H. G., Fiedler, B. & Schulte, K. Influence of different carbon nanotubes on the mechanical properties of epoxy matrix composites—A comparative study. *Compos. Sci. Technol.* **65**, 2300–2313 (2005).
20 Breton, Y., Desarmot, G., Salvetat, J. P., Delpeux, S., Sinturel, C., Beguin, F. & Bonnamy, S. Mechanical properties of multiwall carbon nanotubes/epoxy composites: influence of network morphology. *Carbon* **42**, 1027–1030 (2004).
21 Gojny, F. H., Wichmann, M. H. G., Kopke, U., Fiedler, B. & Schulte, K. Carbon nanotube-reinforced epoxy-compo sites: enhanced stiffness and fracture toughness at low nanotube content. *Compos. Sci. Technol.* **64**, 2363–2371 (2004).
22 Guo, P., Chen, X. H., Gao, X. C., Song, H. H. & Shen, H. Y. Fabrication and mechanical properties of well-dispersed multiwalled carbon nanotubes/epoxy composites. *Compos. Sci. Technol.* **67**, 3331–3337 (2007).
23 Aufray, M. & Roche, A. A. Is gold always chemically passive? Study and comparison of the epoxy-amine/metals interphases. *Appl. Surf. Sci.* **254**, 1936–1941 (2008).
24 Woods, G. *The ICI Polyurethane Book*, (John Wiley & Sons, Inc., New York, NY, USA, 1990).
25 Jelitto, H., Felten, F., Swain, M. V., Balke, H. & Schneider, G. A. Measurement of the total energy release rate for cracks in PZT under combined mechanical and electrical loading. *J. Appl. Mech-T Asme* **74**, 1197–1211 (2007).
26 Rösner, H., Parida, S., Kramer, D., Volkert, C. A. & Weissmüller, J. Reconstructing a nanoporous metal in three dimensions: An electron tomography study of dealloyed gold leaf. *Adv. Eng. Mater.* **9**, 535–541 (2007).
27 Dotzler, C. J., Ingham, B., Illy, B. N., Wallwork, K., Ryan, M. P. & Toney, M. F. In Situ Observation of Strain Development and Porosity Evolution in Nanoporous Gold Foils. *Adv. Funct. Mater.* **21**, 3938–3946 (2011).
28 Qi, Z., Vainio, U., Kornowski, A., Ritter, M., Weller, H., Jin, H. J. & Weissmüller, J. Porous Gold with a Nested-Network Architecture and Ultrafine Structure. *Adv. Funct. Mater.* **25**, 2530–2536 (2015).
29 Huber, N., Viswanath, R. N., Mameka, N., Markmann, J. & Weissmuller, J. Scaling laws of nanoporous metals under uniaxial compression. *Acta Mater.* **67**, 252–265 (2014).
30 Mameka, N., Markmann, J., Jin, H.-J. & Weissmueller, J. Electrical stiffness modulation—confirming the impact of surface excess elasticity on the mechanics of nanomaterials. *Acta Mater.* **76**, 272–280 (2014).
31 Haasen, P. *Physikalische Metallkunde*, (Springer, Berlin, Germany, 1984).
32 Timoshenko, S. *History of Strength of Materials: With a Brief Account of the History of Theory of Elasticity and Theory of Structures*, (Dover Publications, 1983).
33 Sochor, M. *Strength of Materials I*, Vydavatelstvi ČVUT, (2004).
34 Oberg, E., Jones, F. D., Horton, H. L. & Ryffel, H. H. *Machinery's Handbook*, (Industrial Press INC., New York, NY, USA, 2000).
35 Hashin, Z. & Shtrikman, S. A variational approach to the theory of the elastic behaviour of multiphase materials. *J. Mechan. Phys. Solids* **11**, 127–140 (1963).
36 Coleman, J. N., Khan, U., Blau, W. J. & Gun'ko, Y. K. Small but strong: A review of the mechanical properties of carbon nanotube-polymer composites. *Carbon* **44**, 1624–1652 (2006).
37 Rubio-Bollinger, G., Bahn, S. R., Agrait, N., Jacobsen, K. W. & Vieira, S. Mechanical properties and formation mechanisms of a wire of single gold atoms. *Phys. Rev. Lett.* **87** (2001).
38 Wu, B., Heidelberg, A. & Boland, J. J. Mechanical properties of ultrahigh-strength gold nanowires. *Nat. Mater.* **4**, 525–529 (2005).
39 Stalder, A. & Durig, U. Study of yielding mechanics in nanometer-sized Au contacts. *Appl. Phys. Lett.* **68**, 637–639 (1996).
40 Gall, K., Diao, J. K. & Dunn, M. L. The strength of gold nanowires. *Nano Lett.* **4**, 2431–2436 (2004).
41 Rubio, G., Agrait, N. & Vieira, S. Atomic-sized metallic contacts: mechanical properties and electronic transport. *Phys. Rev. Lett.* **76**, 2302–2305 (1996).
42 Kim, K. S., Song, J. Y., Chung, E. K., Park, J. K. & Hong, S. H. Relationship between mechanical properties and microstructure of ultra-fine gold bonding wires. *Mech. Mater.* **38**, 119–127 (2006).
43 Dou, R. & Derby, B. The strength of gold nanowire forests. *Scripta Mater.* **59**, 151–154 (2008).
44 Lee, D., Wei, X., Chen, X., Zhao, M., Jun, S. C., Hone, J., Herbert, E. G., Oliver, W. C. & Kysar, J. W. Microfabrication and mechanical properties of nanoporous gold at the nanoscale. *Scripta Mater.* **56**, 437–440 (2007).
45 Sun, Y., Ye, J., Shan, Z., Minor, A. M. & Balk, T. J. The mechanical behavior of nanoporous gold thin films. *JOM* **59**, 54–58 (2007).
46 Zhong, Y., Markmann, J., Jin, H. J., Ivanisenko, Y., Kurmanaeva, L. & Weissmüller, J. Crack mitigation during dealloying of Au25Cu75. *Adv. Eng. Mater.* **16**, 389–398 (2014).